A data-driven approach to physics-based risk models for deep-seated landslides

Rachael Lau[1], **Manolis Veveakis**[1]

[1]Duke University, Durham, NC 27708

Key Points:

- InSAR displacement readings can reflect sub-surface ground motion
- Spatial interpolation with InSAR can be used to build correlation maps for physics-based outcomes in the shear band
- A physics-based, data-driven risk map can inform risk measures for landslide failure

Corresponding author: Rachael Lau, `rachael.lau@duke.edu`

Abstract

This study addresses the modeling of deep-seated landslides, focusing on the El Forn landslide in Andorra, using remote sensing and data-driven approaches to create risk maps. A temperature-based model is adjusted with data from an instrumented borehole to determine material properties and conditions. The calibrated model is compared to Interferometric Synthetic Aperture Radar (InSAR) data, using the data for spatial analysis and creating a correlation map through kriging. This map leads to a physics-informed risk map indicating areas of instability. An uncertainty analysis of the model highlights its limitations but underscores the utility of such maps for policy and planning in areas prone to landslides. This approach provides a novel tool for assessing landslide risks, combining in-situ and remote sensing data for effective risk management.

Plain Language Summary

In this research, remote sensing and data-driven methods are combined to model deep-seated landslides, focusing on the El Forn landslide in Canillo, Andorra. A temperature-driven physics-based model is calibrated using in-situ data from a borehole in the landslide. The calibrated model was compared with Interferometric Synthetic Aperture Radar (InSAR) data to analyze displacement. InSAR data was also used for spatial interpolation to create a correlation map for the landslide, forming the basis of a physics-based risk map. Despite uncertainties, this risk map, based on a factor of safety, can be a valuable tool for decision-makers in vulnerable regions, providing insights for policy and development initiatives.

1 Introduction

Deep-seated landslides involve the movement of large, slow-moving, masses of soil creeping at often imperceivably slow speeds before catastrophically collapsing(Haque et al., 2019; McColl, 2022; Shuster & Highland, 2001). Driven by a combination of natural and anthropogenic factors, these extreme slope failures events pose significant societal risks, manifesting in both economic losses and human casualties(Haque et al., 2019; Shuster & Highland, 2001). These mass movements slip along a heavily-deformed shearing surface, known as the shear band(Smalley, 1978; Seguí et al., 2020). Because these sliding surfaces are typically made up of clay, they are especially sensitive to pressure and temperature changes(Ghuman & Lal, 1985; Rice, 2006; Veveakis et al., 2007; Seguí et al., 2020; Seguí & Veveakis, 2022; Vardoulakis, 2002; Veveakis et al., 2010). For several decades, these landslides were monitored via borehole instrumentation, which measured parameters such as pore pressure, displacement, and temperature(Uhlemann et al., 2016; Francioni et al., 2021; Gladwin & Hart, 1985). However, drilling and instrumenting these boreholes are invasive, labor-intensive, and expensive – assuming that it is logistically feasible to access these sites, which are often remote and difficult to reach(Francioni et al., 2021; Wasowski & Pisano, 2020). This has motivated a rise in interest in remote sensing techniques for landslide monitoring over the past few decades(Piciullo et al., 2018; Casagli et al., 2023; Scaioni et al., 2014; Zan & Guarnieri, 2006). Light Detection and Ranging (Lidar) and unmanned aerial vehicles (UAV) have been used over the past few decades to build a knowledge bases of remote regions (Kasai et al., 2009). Lidar has helped create topographic maps, creating digital elevation models and understanding potential landslide areas (Baldo et al., 2009; Perski et al., 2014; Ventura et al., 2011; Tiwari et al., 2020). Similarly, UAV have been employed to produce high-resolution image acquisition in photogrammetry, noting areas of risk by comparing changes in aerial images(Mora et al., 2003; Cascini et al., 2009; Mohan et al., 2020). In the last decade, Interferometric Synthetic Aperture Radar (InSAR) has increased in popularity for deep-seated landslide modeling(Bellotti et al., 2014; Bekaert et al., 2020; Jia et al., 2022; Armaș et al., 2021).

InSAR specifically has gained popularity in recent years, with reliable InSAR data available for download and processing via several newly-introduced InSAR processing softwares(Gens & Logan, 2003; Yunjun et al., 2019). InSAR uses radar signals from satellites – in this case, Sentinel-1 – to measure ground surface deformations with high precision (up to 1-2mm of displacement in some cases)(Zhao & Lu, 2018; Lissak et al., 2020). InSAR depends on the principle of interferometry, which compares the phase differences of radar signals between two or more satellite passes over the same area and thereby calculating possible ground displacement values(Osmanoğlu et al., 2016; Bamler & Hartl, 1998; Burgmann et al., 2003). Moreover, InSAR's ability to provide regional perspective with large-scale swaths of radar data makes it an attractive option for regional planning for risk, especially for remote regions who may, in the face of increased risk and exposure to deep-seated landslides, be unable to financially or logistically support the drilling of boreholes for insitu monitoring(Zhang et al., 2018, 2020). As a non-intrusive form of monitoring, InSAR helps remove the need for on-site access to sites of interest. This also removes the risk of drilling excess boreholes in already-deemed unstable regions and further triggering the landslide towards collapse(Hashemi, 2015). Lastly, since radar signals can penetrate clouds, it offers to be a suitable option for monitoring through all weather conditions, as opposed to satellite images(Colesanti & Wasowski, 2006; Samsonov et al., 2013; Wang et al., 2019). The implications of this are particularly notable for communities that experience monsoon seasons in which cloud cover is ever-present and shear bands are being loaded due to rainfall(Meena et al., 2021; Kashyap et al., 2021).

In this paper, we propose an approach that integrates InSAR with insitu borehole data against the backing of a mathematical model in order to create a physics-based risk map for the case study of the El Forn landslide in Andorra. We employ a physics-based model that is driven by temperature evolution in the shear band and calibrate it against insitu borehole data from the El Forn landslide (Seguí et al., 2020, 2021; Seguí & Veveakis, 2021, 2022). The fine-tuned parameters of the model serve as inputs for generating a physics-based blueprint, subsequently compared with ascending track Interferometric Synthetic Aperture Radar (InSAR) data. Additionally, we employ ordinary kriging to create a high-fidelity correlation map for the landslide using the average velocity derived from a time-series inversion of InSAR data during the summer of 2019(Cressie, 1988). We use this correlation map to act as the foundation for a physics-based risk map, established by normalizing the map relative to the pixel containing the location of the instrumented borehole in question. The resulting risk map highlights spatial variations in critical instability based on the underlying predictive physics-based model. Finally, we conduct an uncertainty analysis to understand the limitations of the assumptions inherent to the physics-based approach and linking it with remote sensing data.

2 Materials and Methods

This work considers both physics-based and data-driven approaches to understanding the stability of deep-seated landslides to build out a more holistic understanding of landslide stability assessment. The use of the physics-based model, explained in the next subsection leans on a physics-based approach, while the work of remote sensing is inherently data-driven. We work to merge these two approaches in fine-tuning the physics-based model with insitu and InSAR data.

2.1 Site Overview

The landslide considered in this work is the El Forn deep-seated landslide, nestled in the Pyranees and situated just above the ski town of Canillo in Andorra(Seguí et al., 2020; Torrebadella et al., 2013). The landslide has been the subject of several studies in the past because of its imminent threat to the town of Canillo, and as one of the largest landslides in the Pyrenees(Torrebadella et al., 2011). The landslide's $300 Mm^3$ sliding mass creeps at an average rate of $0.5-2$cm/year and is equipped with 12 boreholes distributed over the entirety of the landslide(Seguí et al., 2021; Seguí & Veveakis, 2021). However, as noted in Seguí and Veveakis (2021), the Cal Ponet-Cal Barronet lobe is a subsection of the sliding mass (approximately $1Mm^3$ sliding mass) that, because it is thought to be moving independently of the larger sliding mass (moving at a faster rate of $1-4$ cm/year), is equipped with more extensive instrumentation. The primary borehole of interest in this study is referred to as "S10", and is equipped with an extensometer, thermometer, and three piezometers. Note that the instrument readings of interest for this work are located at or below the $29m$ depth sliding surface (Seguí et al., 2020). Most notably, the piezometer located below the sliding surface accounts for the fact that this landslide is loaded by a sub-surface aquifer(Seguí et al., 2021). The sliding surface is comprised of 80% Silurian shales and 20% quartz. Figure 1 details the layout of the Cal Ponet-Cal Barronet lobe with respect to the larger El Forn landslide and the town of Canillo (Seguí et al., 2020). More information on the minerology of the sliding surface can be found in Seguí et al. (2020).

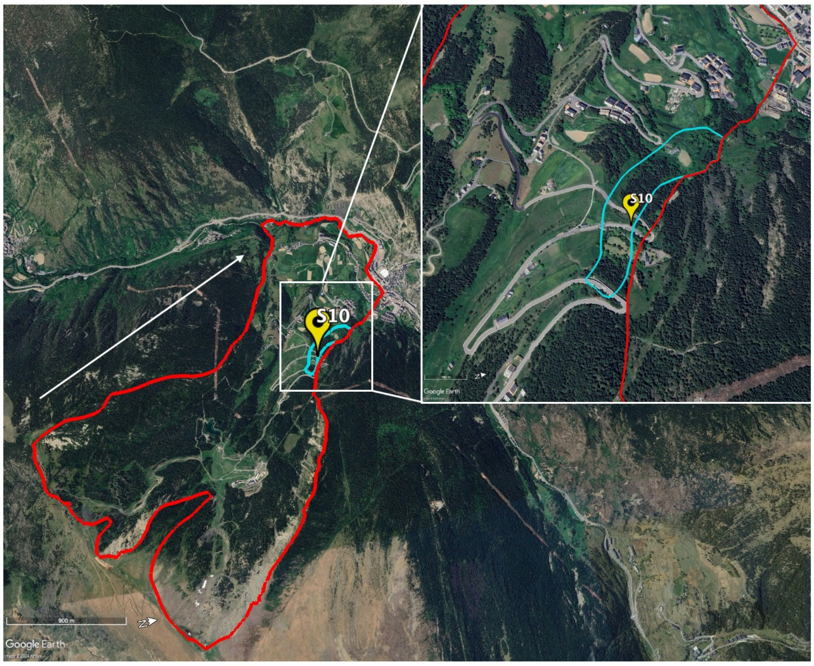

Figure 1. Overview of the El Forn landslide with the encased Cal Ponet–Cal Borronet lobe above Canillo, Andorra. White arrow indicates direction of motion and borehole S10 is marked. (Earth, 2024).

2.2 Physics-based model

The physics-based model considered in this work is a temperature-based approach to forecasting and assessing deep-seated landslide stability, developed by Vardoulakis (2002) and Veveakis et al. (2007) and furthered by Seguí and Veveakis (2022). The constitutive equations for the mathematical model, following the work of (Vardoulakis, 2002), consider a clay material within the shear band of a deep-seated landslide (which moves as a rigid block atop the shear band) experiencing thermal softening (Seguí & Veveakis, 2021, 2022) – equations previously applied to and examined for the case studies of the

Vaiont landslide (Italy) and the Shupping landslide (China)(Seguí et al., 2020; Seguí & Veveakis, 2022; Veveakis et al., 2007) as well as the Reunion landslide in the Italian Alps (Morcioni et al., 2023a, 2023b). The model is presented here briefly for completeness, and the reader is encouraged to refer to the aforementioned works for the full details and assumptions involved.

For this work, key assumptions presented by Seguí et al. (2021) detail that the stress equilibrium inside the shear band necessitates constant profile for the effective stress within the shear band and shear and normal stresses equivalent to the external values, such that $\frac{\delta\sigma'_{xz}}{\delta z} = \frac{\delta\sigma'_{zz}}{\delta z} = 0$, $\sigma'_{xz} = \tau_d(t)$, and $\sigma'_{zz} = \sigma'_n(t)$, respectively. Also, assuming that the clay is at critical state thereby deforming under constant volume, mass balance necessitates a zero volumetric strain. Thus, the main equation then describing the response of the basal material must be the energy equation, such that:

$$\frac{\partial\theta}{\partial t} = c_{th}\frac{\partial^2\theta}{\partial z^2} + \frac{\sigma'_{xz}\dot{\epsilon}_{xz}}{\rho C_m}, \tag{1}$$

with the initial temperature θ being equivalent to the background temperature in the shear band, such that $\theta = \theta_{boundary}$. We assume that $z = -\frac{ds}{2}, \frac{ds}{2}$, where ds is the thickness of the shear band material and z is the direction perpendicular to the sliding direction. ρC_m is the heat capacity of the shear band material, c_{th} is the thermal diffusivity and can be characterized as $c_{th} = \frac{jk_m}{\rho C_m}$, where jk_m is the thermal conductivity. Since El Forn is fed primarily by an aquifer below the shear band, it is assumed that water pressure variations below the shear band directly impact the loading of the landslide (Seguí & Veveakis, 2021). Per the considerations in Seguí and Veveakis (2021) it is then possible to reduce evolution of basal temperature and its relationship with the temperature created through frictional heating by:

$$\frac{\partial\theta^*}{\partial t^*} = \frac{\partial^2\theta^*}{\partial z^{*2}} + Gre^{\theta^*}, z^*\epsilon[-1,1], t > 0 \tag{2}$$

where length z, time t, and temperature θ have been respectively non-dimensionalized, such that:

$$z^* = \frac{z}{\frac{ds}{2}}, t^* = \frac{c_{th}}{(\frac{ds}{2})^2}t, \theta^* = m(\theta - \theta_{boundary}) \tag{3}$$

In this case, m is the relationship between the rate sensitivity coefficient N and the thermal sensitivity coefficient M, such that $m = \frac{M}{N}$. However, Seguí and Veveakis (2021) notes that the minerology of the shear band is the primary driver of the rate sensitivity N, and is the primary considered variable between M and N. The dimensionless group, Gr, commonly known as the Gruntfest number (Seguí et al., 2020), is defined as

$$Gr = G_0\left(1 + \frac{p_f}{p_{f0}}\right)^{(1+1/N)}, \tag{4}$$

with

$$G_0 = m\frac{\dot{\gamma}_{ref}}{jk_m}\frac{ds^2}{4}\tau_{d,ref} \tag{5}$$

The Gruntfest parameter expresses the ratio of the mechanical work converted into heat over the heat diffusion capabilities of the material and captures many of the physical properties of the shear band, including thermal conductivity (jk_m), thermal rate sensitivity N, references shear stress ($\tau_{d,ref}$), thickness of the shear band (ds), and the shear stress applied from external loading sources (Seguí et al., 2020; Gruntfest, 1963). This parameter is the fundamental parameter considered in understanding the critical stability of the deep-seated landslide (Seguí & Veveakis, 2022). For the purposes of being used in conjunction with surface remote sensing data, the model can be furthered reduced by depth averaging inside the shear band, thereby dropping the requirement of depth-related information. Thus, by assuming a parabolic profile of temperature in the shear band via depth averaging leads to:

$$\frac{\partial^2 \theta^*}{\partial z^2} = -\theta^* \tag{6}$$

Equation 2 is then simplified to the following ode:

$$\frac{d\theta^*}{dt^*} = -\theta^* + Gre^{\theta^*} \tag{7}$$

This equation is the guiding equation used to tune the physics-based model with insitu data. However, in order to translate the mathematical model assessment of stability to data derived from InSAR and insitu readings, velocity (and thereby displacement) must also be derived from the strain rate. The work done by Seguí et al. (2020) suggests a visco-plastic flow law for clay-like materials, such that the deviatoric strain rate within the shear band, $\dot{\gamma}$, can be described as:

$$\dot{\gamma} \approx \frac{V - V_0}{ds} \approx \frac{V}{ds} = \dot{\gamma}\left(\frac{\tau_{no}}{\sigma_{ref}}\right)^{1/N} (1 + p^*)^{1/N} e^{\theta^*} \tag{8}$$

or equivalently

$$V = V_0(1 + p^*)^{1/N} e^{\theta^*},\ V_0 = \dot{\gamma} ds \left(\frac{\tau_{no}}{\sigma_{ref}}\right)^{1/N} \tag{9}$$

In order to understand the overall stability of the deep-seated landslide with respect to temperature, the fixed points (steady state solutions) of Equation 7 is resolved (Veveakis et al., 2010; Seguí et al., 2020), such that the Gruntfest parameter can be solved as a function of temperature:

$$Gr = \theta^* e^{-\theta^*} \tag{10}$$

Performing a bifurcation analysis on the mathematical model using Equation 2 (see Seguí et al. (2020), for details), stability of various points on a landslide (and thereby the stability of the landslide itself) can be understood on a Temperature-Gruntfest phase space, as seen in Figure 2. Thermal rate sensitivity, N must be considered nonzero, per Seguí et al. (2021)) in order to have an acceptable reference shear stress of 60 and 180kPa for the 30m depth of the shear band. Using this assumption, for $N \neq 0$, Gruntfest and dimensionless temperature interact along the lower branch of the conditionally stable curve shown in Figure 2, suggesting that if Gr were to pass the critical value at the inflection point on the lower curve, the landslide would become unstable and collapse. Thermal sensitivity necessitates that the mathematical response of the physics-based model will create an option of instability, in which the landslide would transition from stable to tertiary creep and then collapse.

With this model in mind, it is possible to compare insitu data from the S10 borehole with model outputs by comparing temperature data from the thermometer in the borehole with temperature solved from the ordinary differential equation expressed in Equation 7, and tuning values for G_0 and N to determine the best values to use in comparing model outputs – non-dimensionalized and theoretical in nature – with InSAR and insitu data types.

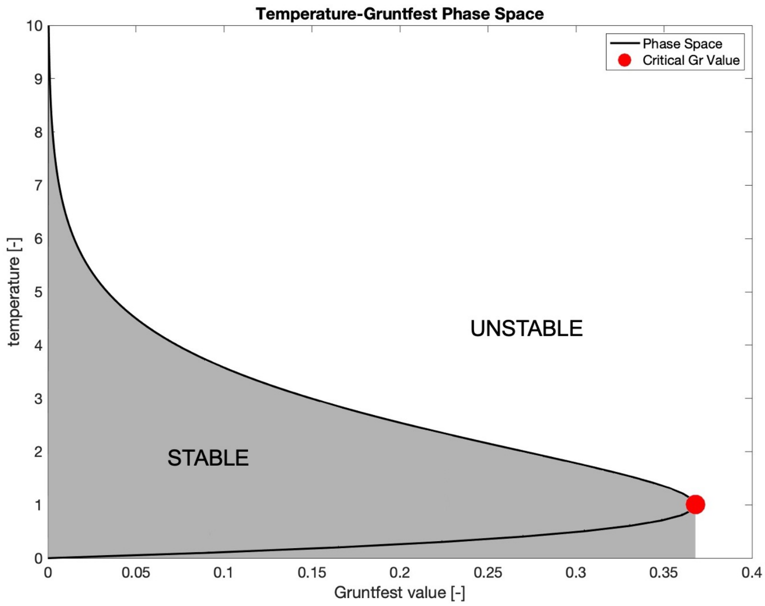

Figure 2. Temperature-Gruntfest phase space, with stable zone shaded in and critical Gruntfest value marked.

2.3 Tuning the physics-based model with insitu data

In order to tune the physics-based model with insitu data values to determine the appropriate N and G_0 value to select to eventually solve for Gruntfest, insitu pore pressure (kPa), temperature (C), and displacement (mm) were selected and non-dimensionalized. Note that, while S10 borehole had multiple piezometers, the piezometer below the shear band was selected in order to reflect the load created by the sub-surface aquifer; there is also only one thermometer in the shear band. Assuming the relationship for $Gr(t)$ reflected in Equation 4, Equation 7 was solved for dimensionless temperature, assuming an initial condition of $\theta_0 = 0$. This ordinary differential equation was iterated over 400 combinations of G_0 and N and compared with the non-dimensionalized temperature readings from S10. Goodness of fit for each combination of G_0 and N were assessed based off of the error criteria:

$$Error = \sum |\theta^*_{field} - \theta^*_{model}| \tag{11}$$

Note that, instrument constraints within the S10 borehole necessitated that the months of May-July 2019 are used for comparative analysis in this work. In order to visualize how error behaves in the system, a mesh of errors was produced, comparing the error of the model and field temperatures for 400 combinations of G_0 and N inputs into the model. As seen in the error mesh in Figure 3, error is minimized along a visible 2-D path (see Figure 3). Local error minima along this path were independently extracted and are seen in Table 1.

In order to narrow down to a single combination G_0 and N, the local minima options (labeled "C1"- "C10") described in Table 1 were each used to solve Equation 7 for non-dimensional temperature θ^*. Through the temperature solution and the pore pressure input, the velocity (derived from the strain rate in the model) can be calculated as:

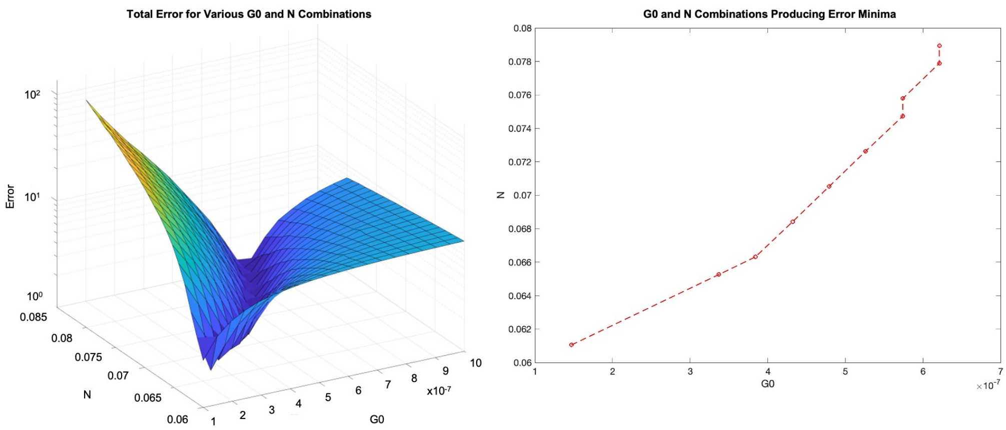

Figure 3. (left) Mesh grid of error results of 400 comparisons between non-dimensionalized field temperature of S10 borehole and solved model for various values of N and G_0.(right)2-D path of local error minima for various G_0 and N combinations.

Table 1. Local error for tuning temperature of model to field, S10

Option Label	G_0 Value	N	Temperature Error
C1	1.474×10^{-7}	6.105×10^{-2}	1.901
C2	3.368×10^{-7}	6.526×10^{-2}	1.915
C3	3.842×10^{-7}	6.632×10^{-2}	1.907
C4	4.637×10^{-7}	6.842×10^{-2}	1.883
C5	4.789×10^{-7}	7.053×10^{-2}	1.891
C6	5.263×10^{-7}	7.263×10^{-2}	1.930
C7	5.737×10^{-7}	7.474×10^{-2}	1.919
C8	5.737×10^{-7}	7.579×10^{-2}	1.929
C9	6.210×10^{-7}	7.789×10^{-2}	1.875
C10	6.210×10^{-7}	7.894×10^{-2}	1.945

$$V^*_{model} = (1 + p^*)^{1/N} e^{\theta^*} \tag{12}$$

with V^*_{model} being the non-dimensional velocity, p^* being the non-dimensional pore pressure from the in-situ data, and θ^* being the non-dimensional temperature output from the model.

From this point, the velocity is integrated in time to solve for non-dimensional model displacement. These displacement time series were then compared against non-dimensional displacement data from the borehole in S10. Visual comparisons of all 10 iterations of both temperature and displacement comparisons for the model and field optimal fits can be found in Figure 4 and Figure 5. While there are slight differences in error between optimized temperature and displacement combinations for G_0 and N, differences in error for all options is relatively negligible. Based off of the fits of both the temperature and displacement readings, we selected option C4, with values $G_0 = 4.637 \times 10^{-7}$ and $N = 6.842 \times 10^{-2}$, and the temperature and displacement outputs for this combination are highlighted in red and the dashed line for temperature and displacement, respectively. This combination aligns with the values that Seguí and Veveakis (2021) retrieved for G_0 and N through laboratory experiments on material collected from the shear band of the landslide and insitu monitoring, and will be used henceforth in the rest of this work. Note, however, that in the absence of constraining information from the site, any G_0 and N value along this line, when used as the two inputs to the physics-based model, will have close alignment with field data. The temperature and displacement comparison plots for the chosen G_0 and N values can be seen in Figures 4 and 5, respectively.

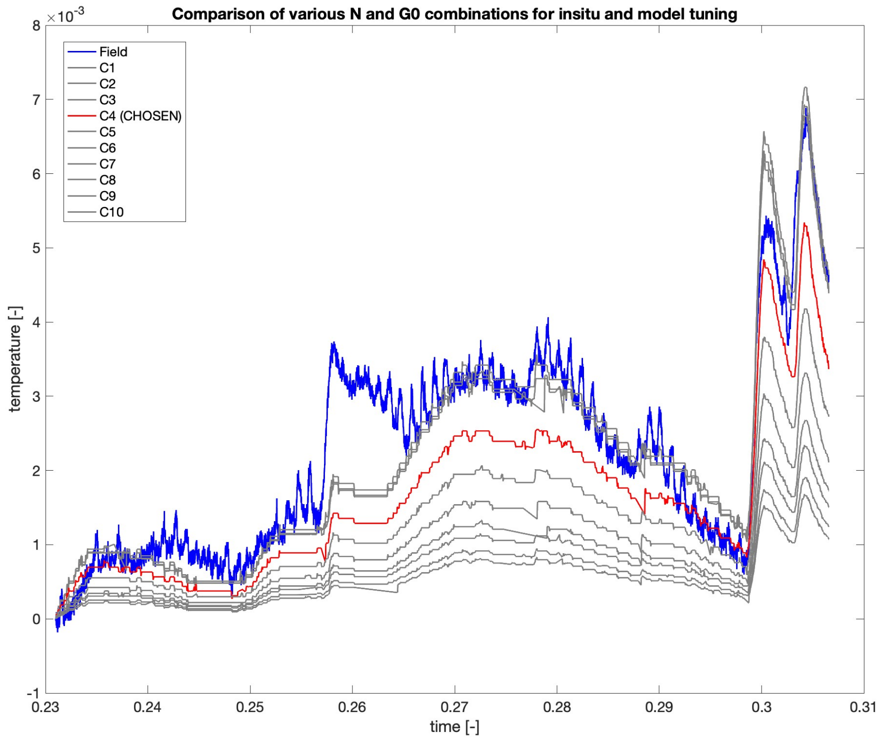

Figure 4. Overall comparison of temperature evolution over time for physics-based model for varying G_0 and N combinations with field data from S10 borehole. The red line reflects the chosen G_0 and N combination, and the blue line indicates the field temperature reading.

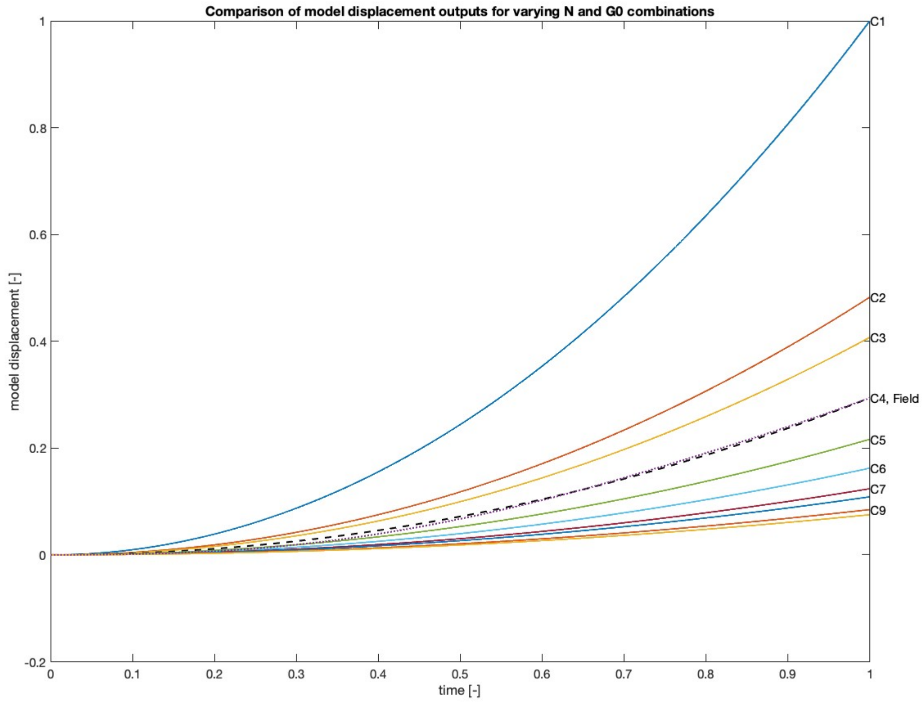

Figure 5. Overall comparison of displacement evolution over time for physics-based model for varying G_0 and N combinations with field data from S10 borehole. Option C4 most closely aligns with the field and is selected moving forward.

2.4 InSAR data collection

For the InSAR data considered in this work, open-access Sentinel-1 C-band ($\sim$5.6 cm radar wavelength) data was retrieved via the Alaska Satellite Facility's (hereinafter referred to as ASF) Vertex Platform's On Demand toolbox (Gens & Logan, 2003; ASF, [Dataset]. Retrieved 2 February 2022). Single Look Complex (SLC) scenes with a beam mode of Interferometric Wide (IW) were selected over the El Forn landslide for the period of the no-snow periods from 2019 with a 6-day acquisition interval on an ascending track (PlanetLab, Retrieved 2019; Gens & Logan, 2003). Once the data has been preprocessed via the ASF Vertex Platform's On Demand toolbox, the resulting stack of interferograms were downloaded via Python script from the ASF Vertex Platform and processed on a computing cluster. Interferograms with visible discontinuities were manually identified and removed from the stack(Gens & Logan, 2003). Each interferogram was then clipped to the same size of overlap using the ASF Hybrid Pluggable Processing Pipeline (Hyp3) toolbox in order to standardize the size of each interferogram for eventual time series inversion. The resulting cleaned, standardized interferogram stack was inverted using the open-source Miami InSAR time-series software for Python (hereinafter referred to as MintPy), using a weighted least squares inversion with a coherence threshold value of 0.4 (Yunjun et al., 2019; Armaș et al., 2021; ASF, [Software]; Yunjun, [Software]). The result of which is a 40x40 meter grid. Note that this data was processed using a high-precision, low-accuracy approach, as opposed to other InSAR retrieval processes (Copernicus, [Dataset]. Retrieved 8 August 2023) in order to ensure higher coverage for the later purposes of spatial data analysis over the lobe (Lau et al., 2024). Further information on this can be found in (Lau et al., 2024) Both individual time series and average velocities were extracted using the Geospatial Data Abstraction Library (GDAL) and MintPy. The output Tag Image File Format (TIFF) file of the average velocity of the no-snow period of 2019 was retrieved and kept aside for spatial data interpolation, and the time series output was deconstructed from a Hierarchical Data Format (in this case, HDF5) file. The time series HDF5 file was deconstructed, with the time series at the index of the S10 borehole extracted, non-dimensionalized, and aligned in time to be compared to the May-July insitu and model readings.

From there, high-resolution (n = 2000 sample points) ordinary-kriging was conducted over the landslide's surface using InSAR average velocity data during the no-snow periods of 2019. The ordinary kriging processes allowed for the creation of a selection of relative values for pixels over the landslide scarp that, because this kriging was conducted at such high-resolution, provides a high-fidelity look at how pixels on the landslide relate to each other solely through the lens of remote sensing (Cressie, 1988). Demonstration of the TIFF file imagery (and the kriged recreation) can be seen in Figure 6. Ordinary kriging was conducted by first creating a grid of x- and y- coordinates and corresponding velocity values at these points. Distances between the random observations and each individual grid point were calculated, such that:

$$d_1 = \sqrt{(x_g - x_{obs}^T)^2 + (y_g - y_{obs}^T)^2}, \tag{13}$$

where x_g and y_g are the grid coordinates, and x_{obs} and y_{obs} are the random observation coordinates. The covariance matrix were determined using the range τ and variance σ^2 from the semivariogram, such that:

$$C = \sigma^2 (e^{(-d_1/\tau)^T}) \tag{14}$$

The euclidean distances between the random observations and each other were calculated, as well as the corresponding covariance matrix Σ, such that:

$$d_2 = \sqrt{(x_{obs} - x_{obs}^T)^2 + (y_{obs} - y_{obs}^T)^2} \tag{15}$$

$$\Sigma = \sigma^2 (e^{(-d_2/\tau)^T}) \tag{16}$$

The covariance matrices were appended into two matrices that would be used Lagrange Multipliers, into matrices Σ' and C', respectively. The weights were calculated by solving the linear equations created by the Σ and C matrices. From there, a predictive correlation matrix Z^* was calculated by taking the values velocity values at the random observations, z_t, multiplying them by the corresponding weights matrix W, such that:

$$Z^* = \Sigma(W \times z_t) \tag{17}$$

3 Results

3.1 G_0 Correlation Map

It is important to note that, while there are two variable inputs to the physics based model described in Section 2.3, G_0 will be the variable of interest used in this work. Since linear dependency between both N and G_0 exists, N is ultimately fixed as $N = 6.842 \times 10^{-2}$. G_0 is an intrinsically varying parameter and better encapsulates the material properties of the landslide (see Equation 5), so it is used the primary variable of interest moving forward in this work. While some of the physical properties of the landslide are captured by the rate sensitivity, assuming a variable N over the landslide would suggest that there are dramatic differences in composition of the sliding material over the landslide,

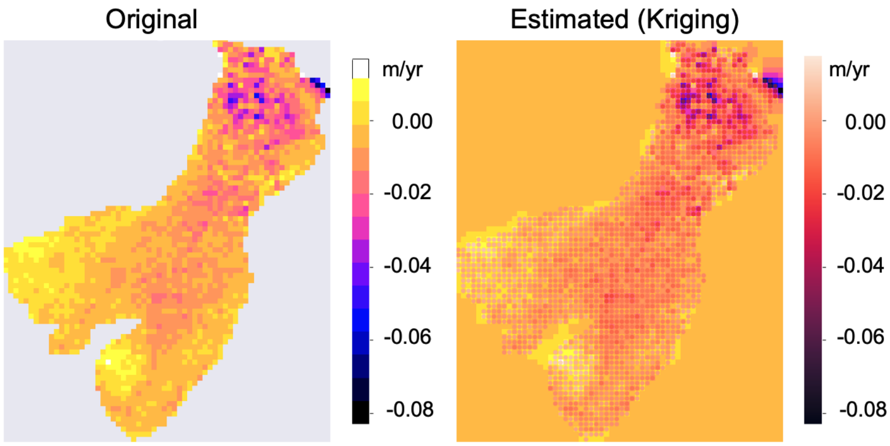

Figure 6. Original and ordinary kriging-based recreation of average velocity over El Forn landslide during May-July 2019.

which goes against the original assumption in the physics-based model of a clay sliding surface.

Assuming a linear relationship between velocity and G_0, the predictive correlation matrix used in the kriging process Z^* summarizes the pixel-to-pixel relationship of the landslide with sample size $n = 2000$ (created through the ordinary kriging process). This weights matrix was normalized to the S10 pixel and made non-negative in order to create a map of G_0. Note that pixels were made non-negative by shifting *all* pixels up by the absolute value of the most negative Z^* value in order to retain the integrity of correlation with respect to the random observations used in creating the kriged model. After this shift, the entire matrix was normalized to the S10 value, such that $Z^*_{S10} = 1$. The entire normalized correlation matrix was used to create the G_0 map, such that:

$$G_{0,matrix} = G_{0,S10} \times Z^* \tag{18}$$

where $G_{0,S10} = 4.637 \times 10^{-7}$, as determined in the model tuning (see Section 2.3). Figure 7 details the resulting G_0 map, with two perspectives: (1) through a top-down view of the landslide, and (2) through a side-on lens of the landslide, showing the fluctuations in G_0 over the landslide. Note that the side-on lens does *not* take into account any other topographical markings other than UTM Coordinates for geospatial positioning (in this case, UTM 31N/EPSG 32631).

3.2 Forecasting

In order to understand the behavior of the physics-based model with respect to InSAR, the InSAR time series for the S10 borehole was extracted from the GDAL and MintPy time series HDF5 file (see Section 2.4) and non-dimensionalized. The displacement InSAR readings were compared to the model output for displacement (see Figure 10 for a model displacement - insitu displacement reading comparison) in order to further ensure the fidelity of the InSAR time series (furthering the work of Lau et al. (2024)). Figure 8 shows this comparison, with the InSAR readings closely following the model displacement.

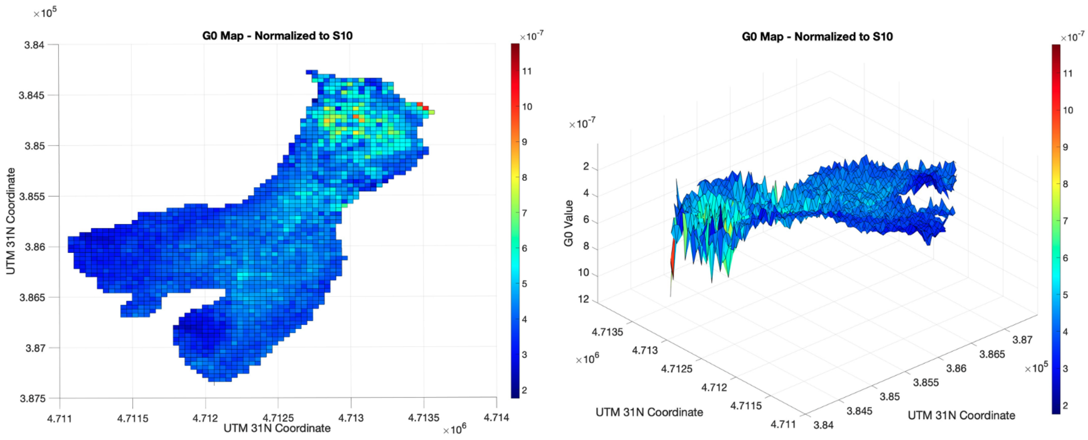

Figure 7. G_0 map, normalized to borehole S10, based off of the correlation matrix of high-fidelity ordinary kriging over the El Forn landslide.

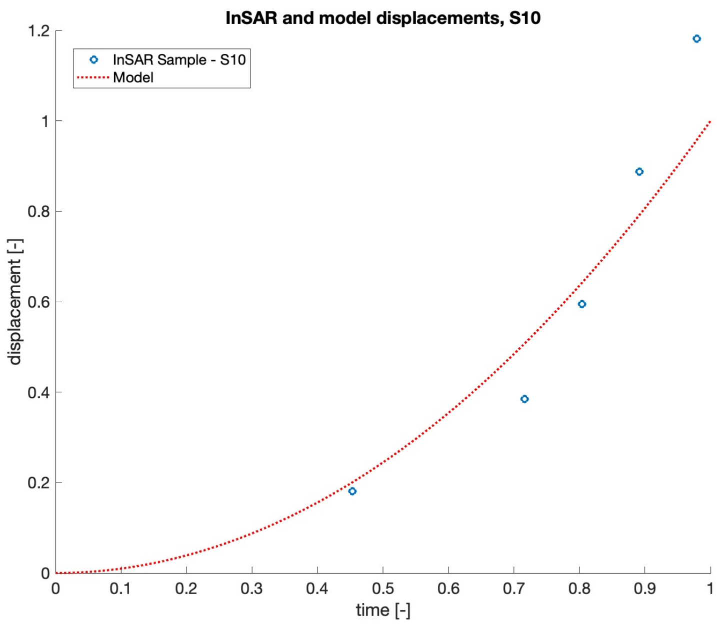

Figure 8. Comparison of model-output displacement for optimized S10 readings and correlated InSAR time series output for S10 pixel.

Given the alignment between InSAR displacement readings and model outputs for S10, five additional points were selected over the lobe in order to understand the behavior of InSAR over the lobe. These samples, named "S1"-"S5", were selected from various points along the landslide in order to understand the variability of the physics-based and data-driven outputs. Table 2 outlines the exact location of each sample, and Figure 9 summarizes their geography along the landslide.

Table 2. Coordinate locations of samples (UTM 31N)

Sample Name	Coordinates
S1	$(384645.13, 4713238.80)$
S2	$(385092.91, 4712957.54)$
S3	$(386027.30, 4712403.30)$
S4	$(386183.72, 4711602.26)$
S5	$(386937.58, 4712222.92)$

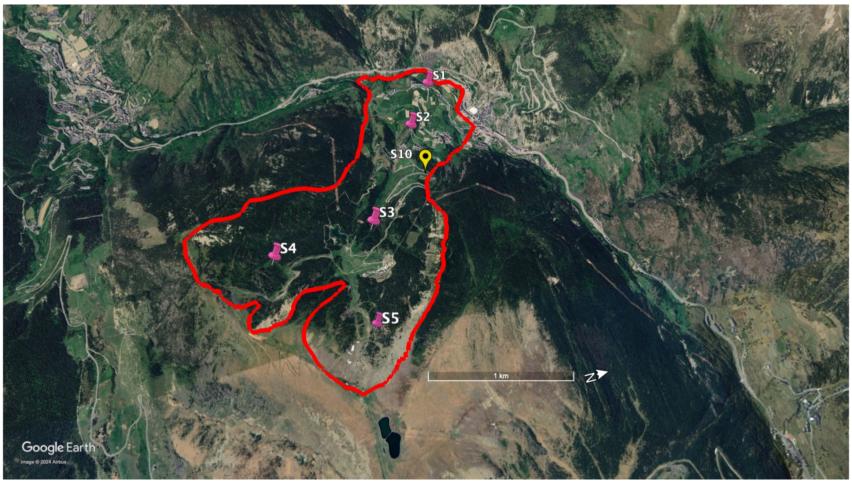

Figure 9. Samples used to confirm physics-based and data-driven assumptions. Samples are labeled S1-S5 and are marked in pink, while the location of S10 is marked in yellow. (Earth, 2024)

The time series for each sample location were extracted from the GDAL and MintPy time series HDF5 file (see Section 2.4) and non-dimensionalized. The G_0 values were pulled out of the S10-normalized G_0 matrix and run individually through the physics-based model with the same rate sensitivity value. The corresponding G_0 values for each sample point are seen in Table 3. In each sample iteration of re-solving Equation 7, the non-dimensional temperature output was similarly used to solve for velocity and subsequently integrated to get the displacement. These model-output displacements were then compared to the InSAR displacement readings, as seen in Supporting Information. Similarly, a comparison of InSAR displacements for S10 with samples S1-S5 be seen in Figure 10. The variations in the displacement readings from InSAR align with the physics of the landslide – samples S4 and S5, located at the crown of the landslide, move much quicker than S10.

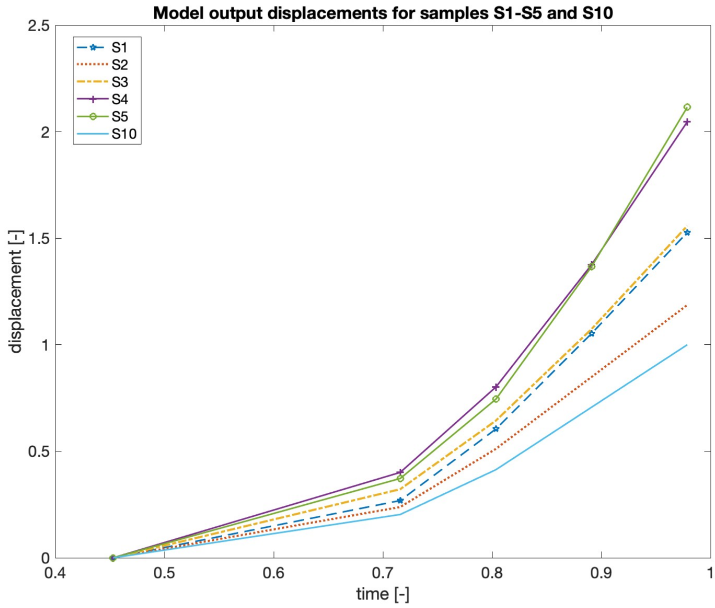

Figure 10. Comparison of InSAR readings for samples S1-S5 with S10.

Table 3. Sample G_0 values extracted from S10-normalized G_0 matrix.

Sample Name	G_0 Value
S1	$5.4683 * 10^{-7}$
S2	$5.3391 * 10^{-7}$
S3	$4.6582 * 10^{-7}$
S4	$3.7253 * 10^{-7}$
S5	$3.8829 * 10^{-7}$

3.3 Uncertainty Quantification

In order to understand and compare the predictability of samples considered in Section 3.2 with respect to S10, the maximum displacement output from the model-output displacement series was compared against the weighted correlation values to S10, which were taken from the correlation matrix derived from the ordinary kriging output Z^* in Section 2.4. These G_0 values, derived from data-driven approaches using InSAR, provide different model-derived maximum displacement value outcomes, summarized in Figure 11. The respective correlation values, which were normalized in relation to S10 (such that $Z^*_{S10} = 1$), fall in line with the expected-physics of the landslide. Samples S4 and S5, located at the crown of the landslide, are expected to exhibit different behavior to the main part of the landslide. This suspected behavior is confirmed by the InSAR displacement value in Figure 11. However, samples S1 and S2, located at the bottom and middle part of the landslide (see Figure 9, can explain the physics of the model and of S10 within a 25% margin of error. Higher uncertainty lies in the crown of the landslide.

This uncertainty is physically explained by the very definition of the quantity G_0 (Equation 5), which is proportional to the landslide's driving stress and therefore to the depth of the sliding mass. Seguí and Veveakis (2021) have estimated the depth of the sliding surface to evolve from a couple of meters at the shallow parts of the crown (top) of the landslide, to 30 meters at the location of the S10 borehole and towards the foot of the landslide. Further to that, the sliding surface has a variable slope, making the driving shear stresses vary considerably across the landslide. These considerations lead the shear stresses acting on the sliding surface to vary from a few kPa at the crown of the landslide all the way to about 400kPa at the foot (Seguí & Veveakis, 2021). Even if we assume that all other material properties of Equation 5 are homogeneous across the landslide, this change of stresses -together with the impossibility of determining the depth of the landslide and whether it moves as a rigid block from the satellite- induces uncertainty in the approach and makes the choice of the calibration point essential for the performance of the work. As a case-in-point, if the model could be validated by in-situ data in the middle of the landslide (sample point 3 in Figure 9), all points would fall within one standard deviation of its displacement.

3.4 Risk Map

Since confirming the fidelity of the InSAR-driven and kriging-based G_0 map with the physics-based model, the Gruntfest parameter G_r, discussed in Section 2.2, is used as the deciding factor to understand both the degree of stability and the initial failure location on the landslide. More specifically, G_0 is one of the key terms used in Equation 4. Using the same sensitivity rate N used through this work, the only other variable of interest is the ratio of pore pressure, such that:

$$p^*_{ratio} = \frac{p_f}{p_{f0}} \tag{19}$$

where the groundwater pressure p_f is compared directly against the background pressure p_{f0}. It is then possible to consider a variety of different scenarios to create a risk map. Depending on the use of this work, it is possible to include a variety of different factors of safety, but for the intents and purposes of this study, a factor of safety (FS) of 1 is used. As such, the Gruntfest value is solved for every pixel of the landslide for a variety of different p^*_{ratio} values. Note that, according to the physics-based model explained in Section 2.2, the critical Gruntfest parameter is $Gr_{crit} = 0.3679$. Therefore, should any solved pixel value of Gruntfest Gr_{pixel} be greater than the critical Gruntfest value Gr_{crit}, the landslide would become unstable and lead to uncontrollable col-

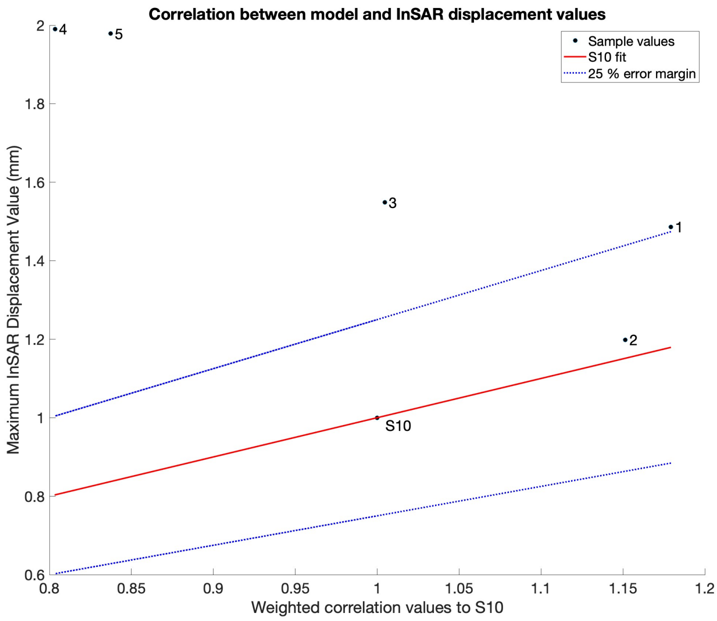

Figure 11. Uncertainty comparison of peak model displacements with correlation to S10 with a 25% error threshold.

lapse. This allows us to define a factor of safety (FS) per pixel, as the ratio

$$FS = \frac{Gr_{crit}}{Gr_{pixel}} \tag{20}$$

This definition in accordance with the classical definition of factor of safety in landslides through the shear stress τ, where $FS = \tau_{cr}/\tau$ (τ_{cr} being the shear resistance). Indeed, Gr is a measure of shear stress (see Equation 4) and the corresponding Factor of Safety of Equation 20 is for all practical purposes formally equivalent to the classical definition when all other parameters are considered constant. The pixel is considered stable when $FS > 1$, critical at $FS = 1$ and unstable when $FS < 1$. For the consideration of the slope's stability, it is not trivial to define an exact measure (norm) of the FS across the field that would correlate exactly with the stability of the entire rock mass. We therefore consider the conservative case of adopting the max norm (i.e. maximum value) of the FS across all pixels of the landslide as an indicator. This implies that if one pixel is unstable the entire slope will be rendered unstable too. This is a very conservative, and to some extend overly restrictive approach since landslides do not become unstable until a critical volume can be mobilized. However, for the qualitative purposes of this work we will introduce the max norm as a metric of stability being aware that future studies will need to focus on defining a less conservative threshold.

Table 4 summarizes the outcomes of a variety of different scenarios for different values of p_{ratio}. Figure 12 details the field maps for the scenaria listed in Table 4, and indicates where in the landslide these critical values of the FS are achieved.For better visualization, the results are plotted for the inverse FS (i.e. stability is ensured for values less than one), while the semi-opaque mesh marks at the final value of criticality, i.e. the plane $FS = 1$. We see that for low values of p^*_{ratio} (1, 1.1 and 1.2) the entire landslide is stable, lying below the critical plane. As the pore pressure ratio increases to 1.3, pixels at the foot of the landslide cross the stability threshold and upon further increase of the pore pressure the entire foot becomes unstable at 1.4 before the entire landslide turns unstable too at higher pore pressures. The results suggest that the deeper parts of the landslide are prone to pore-pressure induced catastrophic instability more than the steepest parts at the crown of the landslide. The latter (steeper parts) are traditionally more susceptible to static slope instability, since steep slopes exceeding the static friction coefficient are intrinsically unstable statically.

Table 4. Summary of landslide stability for various p^*_{ratio} values.

p^*_{ratio}	Landslide Stability
1	Stable
1.1	Stable
1.2	Stable
1.3	UNSTABLE
1.4	UNSTABLE
1.5	UNSTABLE
1.6	UNSTABLE

4 Discussion and Conclusions

This work, in its aim to create quantifiable and accessible risk maps for the post failure evolution and catastrophic collapse of deep-seated landslides, synthesizes high-fidelity insitu borehole data with remote sensing InSAR data, driven by previously-proven physics-based model for forecasting. The work done by Vardoulakis (2002); Veveakis et al. (2007); Seguí et al. (2020) in the development of the physics-based model necessitates two variables, G_0 and N as the two parameters of interest in tuning the physics-based model with borehole data from the El Forn landslide. In order to tune the physics-based model to the insitu data provided in the S10 borehole, over 400 iterations of varying G_0 and N combinations were simulated to solve for the evolution of dimensionless temperature over dimensionless time (see Equation 7). While there was not a global minimum of the 400 iterations, 10 options with local error minima (as seen in Figure 3 and Table 1) were explored further as options "C1"-"C10". Option C4, with $G_0 = 4.637 \times 10^{-7}$ and $N = 6.842 \times 10^{-2}$, was ultimately selected as the optimized variables for the assumed ground truth of S10. While other options provided acceptable fits as well, option C4 offered minimize temperature fit error and a good displacement match with insitu data, as seen in Figures 4 and 5. This combination of G_0 and N became the axis by which we were able to analyze and compare InSAR with corresponding model outputs from other points on the landslide (Yunjun et al., 2019).

Before comparing other points along the landslide, however, we compared the InSAR displacement readings at S10 with the field output displacement readings, confirming that InSAR was indeed reflective of the sub-surface ground motion, further confirming the work done by Lau et al. (2024). Creating a high-fidelity (n=2000 sample points) correlation matrix summarizing each pixel on the scarp and its average-read InSAR velocity for the no-snow periods of 2019 via ordinary kriging allowed us to create a normalized map (for S10) for G_0 along the landslide, assuming a linear relationship between G_0 and velocity(PlanetLab, Retrieved 2019; Cressie, 1988). From there, we were able to extract specific values for G_0 along the scarp while keeping rate sensitivity N constant, as seen in Samples "S1"-"S5" (see Figure 9 and Tables 2, 3). Note that considering a variable rate sensitivity N would imply marked material heterogeneity over the landslide, so G_0 is the variable of interest moving forward. These extracted G_0 values were then used to derive corresponding dimensionless temperature and displacement values by solving equations 7, 9 and integrating for displacement. Similarly, the InSAR time series were

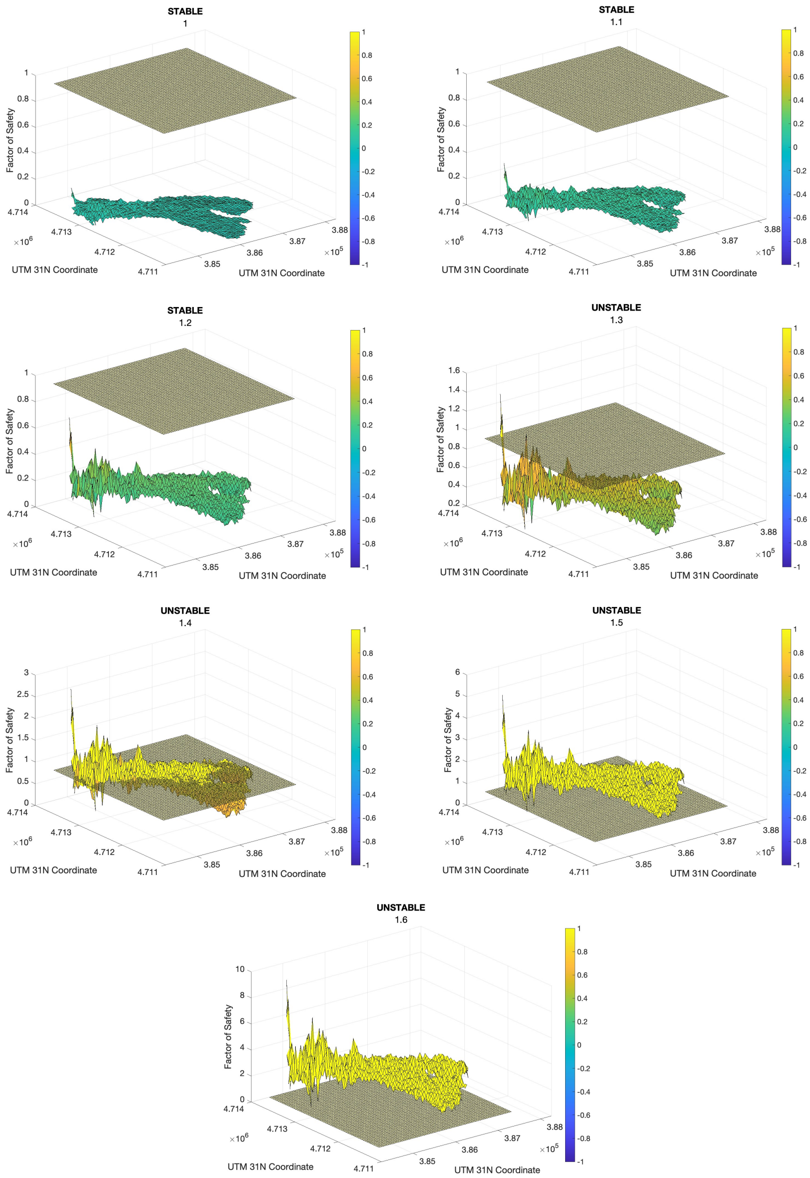

Figure 12. Risk (inverse Factor of Safety) map for various combination of p^*_{ratio} values shown underneath the title of each sub-figure.

compared for each simulated displacement time series for samples S1-S5. The variable displacement outputs in Figure10 align with the spatial variation along the landslide and the varying stresses that different parts of the landslide may experience. After confirming the fidelity of the InSAR data with the physics-based and data-driven outputs for displacement, we were able to create a risk map for different loading scenarios by varying the ratio of current pore pressure to background pore pressure. By solving Equation 4, we were able to solve for the Gruntfest parameter, which through the work of Seguí et al. (2021), can be compared to a critical Gruntfest value that dictates the stability of the landslide Vardoulakis (2002); Gruntfest (1963). By establishing a Gr-based factor-of-safety approach for the mobilised phase of the landslide, we have created a malleable framework for assessing deep-seated landslide conditions over a variety of different loading scenarios.

The correlation between the model and InSAR displacements, meant to be an indicator of sub-surface ground motion, was used to create an uncertainty envelope, as seen in Figure 11. Given that S10, which lies on the periphery of the considered sliding mass, we expected there to be outliers outside the single standard deviation (25%) envelope. However, Figure 11 requires a more in-depth exploration of uncertainty. Since G_0 is considered the variable of interest over the landslide, the variables that comprise it – the ratio of the rate sensitivity and thermal rate m, reference strain rate $\dot{\gamma}_{ref}$, thermal conductivity jk_m, the thickness of the shear band ds, and the reference shear stress $\tau_{d,ref}$ – similarly propagate uncertainty (see equation 5). There are a few key assumptions that may produce uncertainty through employment of the model through linking with InSAR. One of the first key assumptions used in the tuning of this model is a constant pore pressure, such that the pore pressure at borehole S10 is assumed over the entirety of the landslide. While it is true that the landslide is all similarly loaded by a sub-surface aquifer (and a bit of snow melt), there is a high chance that the pore pressure is not geo-spatially homogeneous over the sliding surface. While the physics-based assumptions of material and assumed mineralogy remain constant between the crown and bottom of the landslide (for example, between samples $S1$ and $S4$), the limitations of assuming of constant pore pressure can be explained by the uncertainty envelope summarized in Figure 11. The displacement fits of InSAR of the optimized physics-based model (with selected G_0 and N as seen in Section 2.3) suggests that the G_0 map, created through the InSAR time series inversion process (see Section 2.4) is a reliable metric in reflecting sub-surface ground movement. However, as seen in Figure 11, samples $S4$ and $S5$ lie outside of the 25% threshold of uncertainty of model displacement for the ground truth of S10. Since the relationship between every pixel along the scarp was calculated with respect to S10 via high-fidelity ordinary kriging, two possible explanations exist for outliers $S4$ and $S5$: (1) the assumption of constant pore pressure over the scarp dismisses the depth of the shear surface at the crown, which is likely more shallow than at the location of $S10$ (and thereby also being loaded differently than the shearing surface at $S10$), or (2) the InSAR readings may be limiting in the interferogram creation due to low-coherence value thresholds (0.4 in this case), or in azimuth angles of the InSAR collection due to higher slopes at the crown, which may impede the fidelity of InSAR readings.

Despite these limitations, the proof of correlation with a subsequent risk map based off of a physics-based model but informed by remote sensing has not be completed to this extent for deep-seated landslides and carries exciting implications. Because of it's predication on a factor of safety this tool emerges as an attractive option for decision-makers in vulnerable regions. The framework's use of InSAR (which is open source in data access through data processing) caters to remote, often subsequently highly-vulnerable mountain communities that cannot either logistically drill boreholes for instrumentation or are financially restricted in doing so. For vulnerable populations, these predictive maps have the capacity to become useful tools of empowerment and resilience and shape a local and quantitative response.

Appendix A Open Research

The Sentinel-1 data used for interferogram creation and time series inversion in the study are available for retrieval from the Alaska Satellite Facility Vertex Platform at: `https://search.asf.alaska.edu`. Source files are listed in the appendix for reference. [ASF Interferogram]

Version 1.5.3 of the MintPy used for InSAR time series inversion and is preserved at `https://github.com/insarlab/MintPy`, available via open-access and developed openly on Github.

Version 2 of the Hyp3 used for InSAR time series inversion and is preserved at `https://hyp3-docs.asf.alaska.edu/v2-transition/`, available via the Alaska Satellite Vertex Platform.

Insitu borehole data of the El Forn landslide used in time series comparison is through partnership with the Government of Andorra and is available upon request from the authors.

Acknowledgments
We acknowledge the collaborative efforts of the co-authors for their expertise and contributions to this work. Carolina Seguí, PhD was instrumental furthering the work done by Manolis Veveakis, PhD and Ioannis Vardoulakis, PhD in the development of the physics-based model. Al Handwerger, PhD provided critical resource guidance on the use of InSAR, ISCE+, and MintPy. Financial support from the National Science Foundation, projects CMMI-2042325 and CMMI-2332069, and the Fulbright Program was instrumental in conducting our investigations. We also appreciate the cooperation of the Government of Andorra in providing crucial in-situ data measurements. These combined efforts significantly enhanced the quality and scope of our study. There are no conflicts of interest, financial or affiliatory, on behalf of the authorship.

References

Armaș, I., Gheorghe, M., & Silvaș, G. C. (2021, 6). Shallow landslides physically based susceptibility assessment improvement using insar. case study: Carpathian and subcarpathian prahova valley, romania. *Remote Sensing 2021, Vol. 13, Page 2385*, *13*, 2385. Retrieved from `https://www.mdpi.com/2072-4292/13/12/2385/htmhttps://www.mdpi.com/2072-4292/13/12/2385` doi: 10.3390/RS13122385

ASF. ([Dataset]. Retrieved 2 February 2022). *Alaska satellite facility vertex platform.* Retrieved from `https://search.asf.alaska.edu/`

ASF. ([Software]). *Alaska satellite facility's hybrid pluggable processing pipeline (hyp3), v2.* Retrieved from `https://hyp3-docs.asf.alaska.edu/`

Baldo, M., Bicocchi, C., Chiocchini, U., Giordan, D., & Lollino, G. (2009, 4). Lidar monitoring of mass wasting processes: The radicofani landslide, province of siena, central italy. *Geomorphology*, *105*, 193-201. doi: 10.1016/J.GEOMORPH.2008.09.015

Bamler, R., & Hartl, P. (1998). Synthetic aperture radar interferometry. *Inverse Problems*, *14*, 1-54. doi: 10.1088/0266-5611/14/4/001

Bekaert, D. P., Handwerger, A. L., Agram, P., & Kirschbaum, D. B. (2020, 11). Insar-based detection method for mapping and monitoring slow-moving landslides in remote regions with steep and mountainous terrain: An application to nepal. *Remote Sensing of Environment*, *249*, 111983. doi: 10.1016/J.RSE.2020.111983

Bellotti, F., Bianchi, M., Colombo, D., Ferretti, A., & Tamburini, A. (2014). Advanced insar techniques to support landslide monitoring. *Lecture*

Notes in Earth System Sciences, *0*, 287-290. Retrieved from https://link.springer.com/chapter/10.1007/978-3-642-32408-6_64 doi: 10.1007/978-3-642-32408-6_64/FIGURES/1

Burgmann, R., Rosen, P. A., & Fielding, E. J. (2003, 11). Synthetic aperture radar interferometry to measure earth's surface topography and its deformation. *Annual Review of Earth and Planetary Sciences*, *28*, 169-209. Retrieved from https://www.annualreviews.org/doi/abs/10.1146/annurev.earth.28.1.169 doi: 10.1146/ANNUREV.EARTH.28.1.169

Casagli, N., Intrieri, E., Tofani, V., Gigli, G., & Raspini, F. (2023, 1). Landslide detection, monitoring and prediction with remote-sensing techniques. *Nature Reviews Earth I& Environment 2023 4:1*, *4*, 51-64. Retrieved from https://www.nature.com/articles/s43017-022-00373-x doi: 10.1038/s43017-022-00373-x

Cascini, L., Fornaro, G., & Peduto, D. (2009). Isprs journal of photogrammetry and remote sensing analysis at medium scale of low-resolution dinsar data in slow-moving landslide-affected areas. *ISPRS Journal of Photogrammetry and Remote Sensing*, *64*, 598-611. Retrieved from http://dup.esrin.esa.it doi: 10.1016/j.isprsjprs.2009.05.003

Colesanti, C., & Wasowski, J. (2006, 12). Investigating landslides with space-borne synthetic aperture radar (sar) interferometry. *Engineering Geology*, *88*, 173-199. doi: 10.1016/J.ENGGEO.2006.09.013

Copernicus. ([Dataset]. Retrieved 8 August 2023). *European ground motion service: Ortho – east-west component 2018-2022 (vector), europe, yearly, oct. 2023.* Retrieved from https://sdi.eea.europa.eu/catalogue/srv/api/records/fef95698-bcb5-4e68-9575-f7dbbf835dd7?language=all

Cressie, N. (1988). Spatial prediction and ordinary kriging. *Mathematical Geology*, *20*, 405-421. doi: 10.1007/BF00892986

Earth, G. (2024). *El forn landslide, 42.555546°, 1.608776°, elevation 1832m.* Retrieved from http://www.google.com/earth/index.html

Francioni, M., Stead, D., Sharma, J., Clague, J. A., & Brideau, M. A. (2021, 8). An integrated insar-borehole inclinometer-numerical modeling approach to the assessment of a slow-moving landslide. *Environmental and Engineering Geoscience*, *27*, 287-305. doi: 10.2113/EEG-D-20-00109

Gens, R., & Logan, T. (2003). *Alaska satellite facility software tools: Manual.* Retrieved from https://asf.alaska.edu/wp-content/uploads/2019/02/asf_software_tools.pdf

Ghuman, B. S., & Lal, R. (1985). Thermal conductivity, thermal diffusivity, and thermal capacity of some nigerian soils. *Soil Science*, *139*, 74-80. Retrieved from https://hdl.handle.net/10568/81492 doi: 10.1097/00010694-198501000-00011

Gladwin, M. T., & Hart, R. (1985). *Design parameters for borehole strain instrumentation* (Vol. 123).

Gruntfest, I. J. (1963, 3). Thermal feedback in liquid flow; plane shear at constant stress. *Journal of Rheology*, *7*, 195-207. Retrieved from https://typeset.io/papers/thermal-feedback-in-liquid-flow-plane-shear-at-constant-6v18wnhoe8 doi: 10.1122/1.548954

Haque, U., da Silva, P. F., Devoli, G., Pilz, J., Zhao, B., Khaloua, A., ... Glass, G. E. (2019, 9). The human cost of global warming: Deadly landslides and their triggers (1995–2014). *Science of The Total Environment*, *682*, 673-684. doi: 10.1016/J.SCITOTENV.2019.03.415

Hashemi, S. (2015). *Drilling and maintaining stable unsupported boreholes in poorly cemented sandy formations* (Unpublished doctoral dissertation). The Univeresity of Adelaide.

Jia, H., Wang, Y., Ge, D., Deng, Y., & Wang, R. (2022). Insar study of landslides: Early detection, three-dimensional, and long-term surface displacement estimation-a case of xiaojiang river basin, china. *Remote Sensing*, *14*, 1759. Retrieved from https://doi.org/10.3390/rs14071759 doi: 10.3390/rs14071759

Kasai, M., Ikeda, M., Asahina, T., & Fujisawa, K. (2009, 12). Lidar-derived dem evaluation of deep-seated landslides in a steep and rocky region of japan. *Geomorphology*, *113*, 57-69. doi: 10.1016/J.GEOMORPH.2009.06.004

Kashyap, R., Arvind, Pandey, C., Bikash, & Parida, R. (2021). Spatio-temporal variability of monsoon precipitation and their effect on precipitation triggered landslides in relation to relief in himalayas. *Landslides*, *18*, 1937-1950. Retrieved from https://doi.org/10.1007/s41324-021-00392-8 doi: 10.1007/s41324-021-00392-8

Lau, R., Seguí, C., Waterman, T., Chaney, N., & Veveakis, M. (2024, 2). Insar-informed in-situ monitoring for deep-seated landslides: Insights from el forn (andorra). *EGUsphere*, 1-0. Retrieved from https://egusphere.copernicus.org/preprints/2024/egusphere-2024-212/ doi: 10.48550/ARXIV.2311.01564

Lissak, C., Bartsch, A., Michele, M. D., Gomez, C., Maquaire, O., Raucoules, D., & Roulland, T. (2020). Remote sensing for assessing landslides and associated hazards. *Surveys in Geophysics*, *41*, 1391-1435. Retrieved from https://doi.org/10.1007/s10712-020-09609-1 doi: 10.1007/s10712-020-09609-1

McColl, S. T. (2022, 1). Landslide causes and triggers. *Landslide Hazards, Risks, and Disasters*, 13-41. doi: 10.1016/B978-0-12-818464-6.00011-1

Meena, S. R., Omid, I., Cees, G. I., Westen, J. V., Thimmaiah, I., Nachappa, G., … Sarkar, R. (2021). Rapid mapping of landslides in the western ghats (india) triggered by 2018 extreme monsoon rainfall using a deep learning approach. *Spatial Information Research*, *29*, 857-869. doi: 10.1007/s10346-020-01602-4

Mohan, A., Singh, A. K., Kumar, B., & Dwivedi, R. (2020). Review on remote sensing methods for landslide detection using machine and deep learning. *Transactions on Emerging Telecommunications Technologies*. Retrieved from https://doi.org/10.1002/ett.3998 doi: 10.1002/ett.3998

Mora, P., Baldi, P., Casula, G., Fabris, M., Ghirotti, M., Mazzini, E., & Pesci, A. (2003, 2). Global positioning systems and digital photogrammetry for the monitoring of mass movements: application to the ca' di malta landslide (northern apennines, italy). *Engineering Geology*, *68*, 103-121. doi: 10.1016/S0013-7952(02)00200-4

Morcioni, A., Apuani, T., Cecinato, F., & Veveakis, M. (2023a). Landslide susceptibility evaluation in alpine environment: 1. 3d finite element modeling of the ruinon (it) case study. *Geomechanics for Energy and the Environment*, *36*, 100493. Retrieved from https://www.sciencedirect.com/science/article/pii/S235238082300062X doi: https://doi.org/10.1016/j.gete.2023.100493

Morcioni, A., Apuani, T., Cecinato, F., & Veveakis, M. (2023b). Landslide susceptibility evaluation in alpine environment: 2. thermo-hydro-mechanical modeling for the response to climate-related variables. *Geomechanics for Energy and the Environment*, *36*, 100494. Retrieved from https://www.sciencedirect.com/science/article/pii/S2352380823000631 doi: https://doi.org/10.1016/j.gete.2023.100494

Osmanoğlu, B., Sunar, F., Wdowinski, S., & Cabral-Cano, E. (2016, 5). Time series analysis of insar data: Methods and trends. *ISPRS Journal of Photogrammetry and Remote Sensing*, *115*, 90-102. doi: 10.1016/J.ISPRSJPRS.2015.10.003

Perski, Z., Wojciechowski, T., & Borkowski, A. (2014). Monitoring of landslide dynamics with lidar, sar interferometry and photogrammetry. case study of kłodne landslide (southern poland).. Retrieved from https://www.researchgate.net/publication/335773123

Piciullo, L., Calvello, M., & Cepeda, J. M. (2018, 4). Territorial early warning systems for rainfall-induced landslides. *Earth-Science Reviews*, *179*, 228-247. doi:

10.1016/J.EARSCIREV.2018.02.013

PlanetLab. (Retrieved 2019). *Planet application program interface: In space for life on earth.* Retrieved from https://www.planet.com/explorer/

Rice, J. R. (2006). Heating and weakening of faults during earthquake slip. *Journal for Geophysical Research*, *111*, 5311. Retrieved from https://agupubs.onlinelibrary.wiley.com/doi/10.1029/2005JB004006 doi: 10.1029/2005JB004006

Samsonov, S., d'Oreye, N., & Smets, B. (2013, 8). Ground deformation associated with post-mining activity at the french–german border revealed by novel insar time series method. *International Journal of Applied Earth Observation and Geoinformation*, *23*, 142-154. doi: 10.1016/J.JAG.2012.12.008

Scaioni, M., Longoni, L., Melillo, V., & Papini, M. (2014). remote sensing remote sensing for landslide investigations: An overview of recent achievements and perspectives. *Remote Sens*, *6*, 1. Retrieved from www.mdpi.com/journal/remotesensing doi: 10.3390/rs60x000x

Seguí, C., Rattez, H., & Veveakis, M. (2020, 7). On the stability of deep-seated landslides. the cases of vaiont (italy) and shuping (three gorges dam, china). *Journal of Geophysical Research: Earth Surface*, *125*. Retrieved from https://www.researchgate.net/publication/341685895_On_the_Stability_of_Deep-Seated_Landslides_The_Cases_of_Vaiont_Italy_and_Shuping_Three_Gorges_Dam_China doi: 10.1029/2019JF005203

Seguí, C., Tauler, E., Planas, X., Moya, J., & Veveakis, M. (2021, 1). The interplay between phyllosilicates fabric and mechanical response of deep-seated landslides. the case of el forn de canillo landslide (andorra). *Landslides*, *18*, 145-160. doi: 10.1007/S10346-020-01492-6

Seguí, C., & Veveakis, M. (2021, 12). Continuous assessment of landslides by measuring their basal temperature. *Landslides*, *18*, 3953-3961. Retrieved from https://link.springer.com/article/10.1007/s10346-021-01762-x doi: 10.1007/S10346-021-01762-X/FIGURES/3

Seguí, C., & Veveakis, M. (2022, 12). Forecasting and mitigating landslide collapse by fusing physics-based and data-driven approaches. *Geomechanics for Energy and the Environment*, *32*, 100412. doi: 10.1016/J.GETE.2022.100412

Shuster, R. L., & Highland, L. M. (2001). *Socioeconomic and environmental impacts of landslides in the western hemisphere.*

Smalley, I. J. (1978, 4). Rockslides and avalanches. *Nature 1978 272:5654*, *272*, 654-654. Retrieved from https://www.nature.com/articles/272654b0 doi: 10.1038/272654b0

Tiwari, A., Narayan, A. B., Dwivedi, R., Dikshit, O., & Nagarajan, B. (2020, 4). Monitoring of landslide activity at the sirobagarh landslide, uttarakhand, india, using lidar, sar interferometry and geodetic surveys. *Geocarto International*, *35*, 535-558. doi: 10.1080/10106049.2018.1524516

Torrebadella, J., Altimir, J., & Villaro, I. (2013). El forn landslide. an example of geological risk management in large sliding inhabited areas. *Landslide Science and Practice: Risk Assessment, Management and Mitigation*, *6*, 323-327. Retrieved from https://link.springer.com/chapter/10.1007/978-3-642-31319-6_43 doi: 10.1007/978-3-642-31319-6_43/FIGURES/00436

Torrebadella, J., Altimir, J., & Villaró, I. (2011). El forn landslide (andorra), an example of geological risk management in large sliding inhabited areas. *Geophysical Research Abstracts*, *13*, 2011-1409.

Uhlemann, S., Smith, A., Chambers, J., Dixon, N., Dijkstra, T., Haslam, E., ... Mackay, J. (2016, 1). Assessment of ground-based monitoring techniques applied to landslide investigations. *Geomorphology*, *253*, 438-451. doi: 10.1016/J.GEOMORPH.2015.10.027

Vardoulakis, I. (2002, 6). Steady shear and thermal run-away in clayey gouges. *International Journal of Solids and Structures*, *39*, 3831-3844. doi: 10.1016/

S0020-7683(02)00179-8

Ventura, G., Vilardo, G., Terranova, C., & Sessa, E. B. (2011, 12). Tracking and evolution of complex active landslides by multi-temporal airborne lidar data: The montaguto landslide (southern italy). *Remote Sensing of Environment*, *115*, 3237-3248. doi: 10.1016/J.RSE.2011.07.007

Veveakis, E., Alevizos, S., & Vardoulakis, I. (2010, 9). Chemical reaction capping of thermal instabilities during shear of frictional faults. *Journal of the Mechanics and Physics of Solids*, *58*, 1175-1194. Retrieved from `www.elsevier.com/locate/jmps` doi: 10.1016/j.jmps.2010.06.010

Veveakis, E., Vardoulakis, I., & Toro, G. D. (2007). Thermoporomechanics of creeping landslides: The 1963 vaiont slide, northern italy. *Journal for Geophysical Research*, *112*, 3026. Retrieved from `https://agupubs.onlinelibrary.wiley.com/doi/10.1029/2006JF000702` doi: 10.1029/2006JF000702

Wang, Y., Wang, X., & Jian, J. (2019). Remote sensing landslide recognition based on convolutional neural network. *Mathematical Problems in Engineering*. Retrieved from `https://doi.org/10.1155/2019/8389368` doi: 10.1155/2019/8389368

Wasowski, J., & Pisano, L. (2020). Long-term insar, borehole inclinometer, and rainfall records provide insight into the mechanism and activity patterns of an extremely slow urbanized landslide. *Landslides*, *17*, 445. Retrieved from `http://www.protezionecivile.puglia.it` doi: 10.1007/s10346-019-01276-7

Yunjun, Z. ([Software]). *The miami insar time-series software in python.* Retrieved from `https://github.com/insarlab/MintPy`

Yunjun, Z., Fattahi, H., & Amelung, F. (2019, 12). Small baseline insar time series analysis: Unwrapping error correction and noise reduction. *Computers and Geosciences*, *133*, 104331. Retrieved from `https://miami.pure.elsevier.com/en/publications/small-baseline-insar-time-series-analysis-unwrapping-error-correc` doi: 10.1016/J.CAGEO.2019.104331

Zan, F. D., & Guarnieri, A. M. (2006, 9). Topsar: Terrain observation by progressive scans. *IEEE Transactions on Geoscience and Remote Sensing*, *44*, 2352-2360. doi: 10.1109/TGRS.2006.873853

Zhang, Y., Meng, X., Colm, I., I, J., Novellino, A., Dijkstra, T., & Chen, G. (2018). Investigating slow-moving landslides in the zhouqu region of china using insar time series. *Landslides*, *15*, 1299-1315. doi: 10.1007/s10346-018-0954-8

Zhang, Y., Meng, X. M., Dijkstra, T. A., Jordan, C. J., Chen, G., Zeng, R. Q., & Novellino, A. (2020, 5). Forecasting the magnitude of potential landslides based on insar techniques. *Remote Sensing of Environment*, *241*, 111738. doi: 10.1016/J.RSE.2020.111738

Zhao, C., & Lu, Z. (2018). Remote sensing of landslides—a review. *Remote Sensing*, *10*(2). Retrieved from `https://www.mdpi.com/2072-4292/10/2/279` doi: 10.3390/rs10020279